Accepted Manuscript

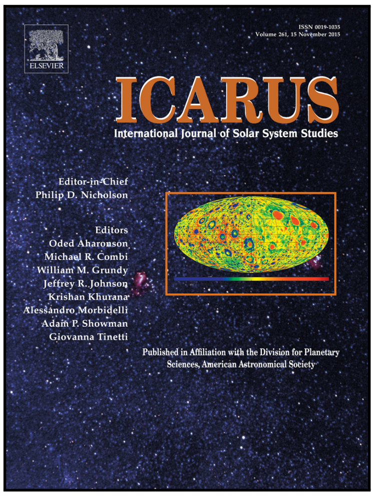

Spheroidal models of the exterior gravitational field of asteroids Bennu and Castalia

Josef Sebera, Aleš Bezděk, Ivan Pešek, Tomáš Henych

PII: S0019-1035(16)00116-0
DOI: 10.1016/j.icarus.2016.02.038
Reference: YICAR 11957

To appear in: *Icarus*

Received date: 28 May 2015
Revised date: 21 January 2016
Accepted date: 22 February 2016

Please cite this article as: Josef Sebera, Aleš Bezděk, Ivan Pešek, Tomáš Henych, Spheroidal models of the exterior gravitational field of asteroids Bennu and Castalia, *Icarus* (2016), doi: 10.1016/j.icarus.2016.02.038

Highlights

- The gravitational field of the shape model is converted to the oblate and the prolate spheroidal harmonic representation
- High-frequency effects are mitigated by increasing the maximum degree
- The behavior of the harmonic series is studied near the Brillouin spheroid
- Gravitational field data sets for Bennu and Castalia are provided

Spheroidal models of the exterior gravitational field of asteroids Bennu and Castalia

Josef Sebera[a,b,*], Aleš Bezděk[a], Ivan Pešek[c], Tomáš Henych[a]

[a] *Astronomical Institute, Academy of Sciences, Ondřejov, The Czech Republic*
[b] *Research Institute of Geodesy, Cartography and Topography, Zdiby, The Czech Republic*
[c] *101 00 Prague, Czech Republic*

Abstract

Gravitational field of small bodies can be modelled e.g. with mascons, a polyhedral model or in terms of harmonic functions. If the shape of a body is close to the spheroid, it is advantageous to employ the spheroidal basis functions for expressing the gravitational field. Spheroidal harmonic models, similarly to the spherical ones, may be used in navigation and geophysical tasks. We focus on modelling the exterior gravitational field of oblate-like asteroid (101955) Bennu and prolate-like asteroid (4769) Castalia with spheroidal harmonics. Using the Gauss-Legendre quadrature and the spheroidal basis functions, we converted the gravitational potential of a particular polyhedral model of a constant density into the spheroidal harmonics. The results consist of i) spheroidal harmonic coefficients of the exterior gravitational field for the asteroids Bennu and Castalia, ii) spherical harmonic coefficients for Bennu, and iii) the first and second-order Cartesian derivatives in the local spheroidal South-East-Up frame for both bodies. The spheroidal harmonics offer biaxial flexibility (compared with spherical harmonics) and low computational costs that allow high-degree expansions (compared with ellipsoidal harmonics). The obtained spheroidal models for Bennu and Castalia represent the exterior gravitational field valid on and outside the Brillouin spheroid but they can be used even under this surface. For Bennu, 5 metres above the surface the agreement with point-wise integration was 1% or less, while it was about 10% for Castalia due to its more irregular shape. As the shape models may produce very high frequencies, it was crucial to use higher maximum degree to reduce the aliasing. We have used the maximum degree 360 to achieve 9–10 common digits (in RMS) when reconstructing the input (the gravitational potential) from the spheroidal coefficients. The physically meaningful maximum degree may be lower (<< 360) but its particular value depends on the distance and/or on the application (navigation, exploration, etc.).

Keywords: Asteroids, surfaces, Near-Earth objects, Geophysics

1. Introduction

Gravitational field of small bodies plays a significant role in a number of phenomena associated with their exploration and dynamics. For example, accurate gravitational fields are used to constrain geophysical investigations or they are used for orbit determination (navigation) of other objects in the body's neighborhood. Werner & Scheeres (1996) overview the main approaches to express planetary gravity fields; mascons, polyhedral (or shape) models and harmonic representations. Each of them has its own drawbacks and advantages; a more detailed comparison can be found in Balmino (1994); Werner & Scheeres (1996); Takahashi & Scheeres (2014) and others.

This contribution belongs to a family of harmonic modelling, we focus on the exterior gravitational field of two small bodies. There are multiple options when using the harmonic functions. Most straightforward is to use spherical harmonics, as they are not computationally demanding (e.g., they can be evaluated up to ultra high degrees $> 10^4$). However, for accurate computations these functions do not suit to irregular bodies such as small bodies because their corresponding spherical Brillouin surface may be too far from the body so the series may not converge (or converge slower) under this surface. The exception are the solutions that employ spherical harmonics in a more sophisticated way; e.g., see Takahashi et al. (2013); Takahashi & Scheeres (2014). On the other hand, instead of spherical harmonics one can employ the ellipsoidal harmonics. Basically, they provide triaxial flexibility, which is very suitable for more irregular shapes. Recently, these functions were applied to the gravitational field of Eros (Garmier et al., 2002), Vesta (Park et al., 2014) and Martian moons (Hu & Jekeli, 2014). However, the computation of ellipsoidal harmonics is not so straightforward and can be numerically demanding; for example, in Park et al. (2014, p.119) it is discussed a use of quadruple precision for stable evaluations of these harmonics about degree 24.

A reasonable trade-off between the spherical and ellipsoidal harmonics is provided by the spheroidal harmonics. Although they offer only biaxial flexibility (oblate and prolate spheroidal harmonics), their computation is not so demanding and one can obtain very high degrees (say $> 10^4$ depending on the flattening). Hence, we may expect the same computational costs as with the spherical harmonics but better performance near the surface of more irregular (non-spherical) bodies. Recently, the computation of spheroidal harmonics or the associated Legendre functions of the second kind was the sub-

*Corresponding author
Email address: sebera@asu.cas.cz (Josef Sebera)

ject of many authors, e.g. (Gil & Segura, 1998), (Segura & Gil, 1999), (Fukushima, 2013, 2014). Here, we use hypergeometric functions and standard definitions from Hobson (1931); Abramowitz et al. (1965), their description is given in Appendix A. The possibility to reach higher degrees becomes important when converting the gravitational fields from shape (polyhedral) models to harmonic representations. This is because, as pointed out in Takahashi & Scheeres (2014, p. 172), the polyhedral gravity signal may generate information of infinitely high degrees and orders. As shown below, by using high-degree expansions of spheroidal harmonics such aliasing can be successfully mitigated. The oblate spheroidal harmonics are traditionally used in Earth and planetary sciences such as geomagnetism, geodesy etc; e.g., Winch (1967); Maus (2010); Lowes & Winch (2012); Pavlis et al. (2012). However, as shown in Fukushima (2014), there are plenty of non-spherical small bodies, to which also prolate spheroidal harmonics are applicable.

Following the motivation from Fukushima (2014) and the choice of the target small bodies in Takahashi & Scheeres (2014), we employ the spheroidal harmonics to express the gravitational field of two small bodies; the oblate-like asteroid (101955) Bennu and the prolate-like asteroid (4769) Castalia. The resulting spheroidal models are based on available shape models of both bodies with a given density. Although assuming the constant density may be limiting, the obtained harmonic models can provide a suitable starting point for further geophysical and navigational tasks. One obvious advantage of the harmonic representation is that the series allows for spectral filtering, which can support further geophysical exploration of short-wavelength structures such as impact basins Zuber et al. (1994); Smith et al. (2012), eliminating the effect of topography for crust and mantle modelling (Wieczorek et al., 2013) etc. For the illustration, Appendix B provides plots of the Cartesian derivatives from the spheroidal harmonic degree 5. All the input data, the resulting gravitational field models and data grids are provided at http://galaxy.asu.cas.cz/planets/index.php?page=sgfm.

2. (101955) Bennu

This Apollo Near Earth Asteroid (NEA) is the primary target of the OSIRIS-REx Asteroid Sample Return Mission (Drake et al., 2011). The prime objective of the mission is to measure Yarkovsky effect on this asteroid (Chesley et al. 2014) and also to investigate physical, mineralogical and chemical properties and to return samples of its material (Lauretta et al. 2014). The spacecraft will also be used to measure Bennu's gravity field by means of radio science (Scheeres et al. 2012).

(101955) Bennu was discovered in September 1999 by the LINEAR survey (former designation 1999 RQ_{36}). Later on, it turned out to be a Potentially Hazardous Asteroid with possible impacts in the second half of the next century (Milani et al. 2009). It was closely observed in optical and infrared bands and also by Arecibo and Goldstone radars in its last three apparitions. Therefore, we have detailed knowledge of some of its physical characteristics. The mean diameter of Bennu is 492 ± 20 m (the dimensions of the three principal axes being, respectively, 565 ± 10 m, 535 ± 10 m and 508 ± 52 m). Its shape

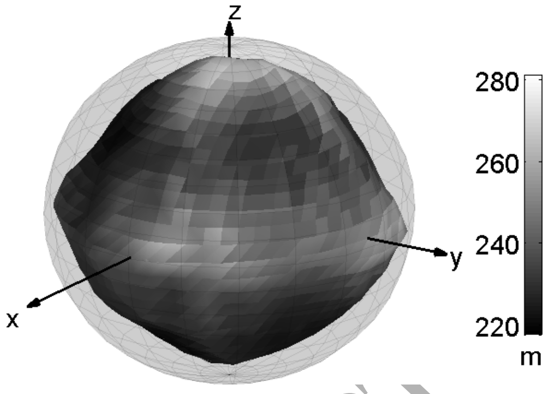

Figure 1: Shape model for Bennu (a polyhedron with triangular facets) and the bounding oblate spheroid with semiaxes from Table 2 (the colorbar indicates the distance from the origin).

resembles that of 1999 KW_4 primary (Ostro et al. 2006), but there is no satellite larger than 15 m (Nolan et al. 2013). The reflectance spectra indicate that Bennu is a primitive B-type asteroid (Clark et al. 2011) with low albedo of $4.5 \pm 0.5\%$ (Lauretta et al. 2014).

The precise shape model, taken from Planetary Data System[1] (PDS), is a result of radar delay-Doppler observation and lightcurve observations (Nolan et al., 2013). Its volume is $0.0623 \pm 0.006\ \mathrm{km}^3$ (ibid). Together with infrared observations, it was possible to estimate its mass and bulk density with high accuracy. The derived bulk density is $1260 \pm 70\ \mathrm{kg/m}^3$ and since the likely meteorite analog density is known, the macroporosity was estimated as $40 \pm 10\%$ (Chesley et al. 2014).

3. (4769) Castalia

(4769) Castalia is also an Apollo NEA. It was discovered in August 1989 at the Palomar Observatory as 1989 PB and observed by radar shortly after its discovery (Ostro et al. 1990). Later, a detailed shape model (Neese, 2004) was obtained from radar observations published by Hudson & Ostro (1994) and it is also available at PDS[2]. It is a bifurcated object consisting of two irregular, kilometer-sized lobes with a volume of $0.6678\ \mathrm{km}^3$. We assume it has a mean density of $2100 \pm 400\ \mathrm{kg/m}^3$ (Scheeres et al. 1996) and rather high porosity of 40% to 60% depending on the meteorite analog density assumption. The accuracy of the shape model is not known but discussed in Hudson & Ostro (1994).

4. Spheroidal modelling of the exterior gravitational field

Since the density variations of Bennu and Castalia are not known, we shall assume these bodies are of a constant density given in the preceding sections. With a constant density, the spheroidal modelling becomes quite straightforward. We start with Eq. (1), with which one can obtain the gravitational

[1] http://sbn.psi.edu/pds/resource/bennushape.html
[2] http://sbn.psi.edu/pds/resource/rshape.html

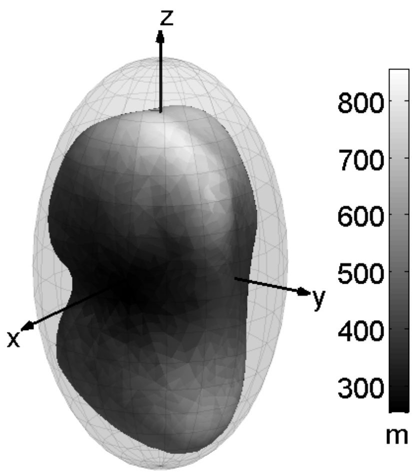

Figure 2: Shape model for Castalia (a polyhedron with triangular facets) and the bounding prolate spheroid with semiaxes from Table 2 (the colorbar indicates the distance from the origin).

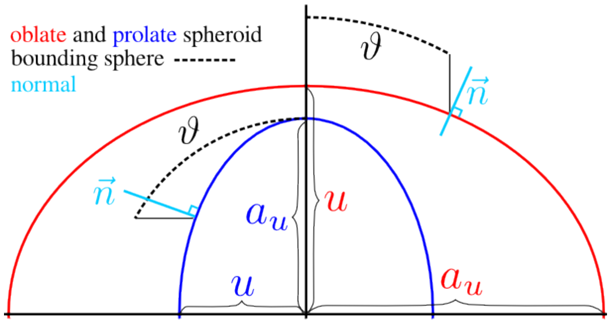

Figure 3: Oblate and prolate spheroids and the convention for denoting the semi-axes. The symbol u denotes always the smaller axis of the spheroid while a_u denotes the second one, ϑ is the polar angle on the bounding sphere.

potential on an arbitrary surface by integrating over a polyhedral shape model of the asteroid. In our case, we have chosen the surfaces of the oblate and the prolate spheroid depicted in Figures 1, 2. The lengths of the semi-axes were chosen to encompass the small body by the spheroid, whose surface is kept close to the body (its shape model). The harmonic coefficients are obtained by the spheroidal harmonic analysis applied to the potential computed with Eq. (1); see Section 4.2. The choice of the gravitational potential for the analysis is customary and one can employ other variable based on Eq. (1). The result of the analysis is a set of the harmonic coefficients called the spheroidal model of the exterior gravitational field. With these harmonic coefficients various gravity field data can be obtained by the spheroidal synthesis; Appendix B gives the relevant relations for the first and second Cartesian derivatives of the gravitational potential that can be used with Eq. (2).

Before we proceed with the analysis, it will be useful to introduce the adopted convention for the spheroid. Start with a relation between the (global) Cartesian and the spheroidal coordinates from Table 1, for which we use the convention depicted in Figure 3. The smaller semi-axis is always denoted by u, while the larger semi-axis has the length equal to a_u. The rotational symmetry is evident from Figure 3 and Table 1.

Table 1: Relation between the Cartesian and the spheroidal coordinates, where $\vartheta \in [0, \pi]$ is the polar angle, $\lambda \in [0, 2\pi)$ is the azimuth, u is always the smaller semi-axis compared with a_u as shown in Figure 3. The quantity $E^2 = a_u^2 - u^2$ is usually called the numerical eccentricity.

Coordinate	Oblate	Prolate
x_1	$\sqrt{u^2 + E^2} \sin\vartheta \cos\lambda$	$u \sin\vartheta \cos\lambda$
x_2	$\sqrt{u^2 + E^2} \sin\vartheta \sin\lambda$	$u \sin\vartheta \cos\lambda$
x_3	$u \cos\vartheta$	$\sqrt{u^2 + E^2} \cos\vartheta$

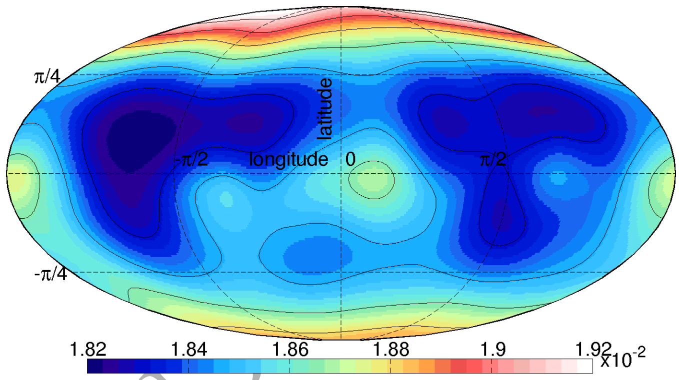

Figure 4: Gravitational potential on the outer spheroid for Bennu computed with Eq. (1) – the input signal to the harmonic analysis (in $m^2 s^{-2}$).

4.1. Gravitational potential from the shape model

Assuming a constant density, the gravitational potential of a small body can be calculated by a surface integration (Werner & Scheeres, 1996, Eq.1)

$$V = \frac{G\rho}{2} \iint_S \vec{n} \cdot \vec{r} \, \mathrm{d}S, \tag{1}$$

where G is the gravitational constant, ρ is the density of a body and the vector $\vec{n}$ and $\vec{r}$ is the normal and the radius vector, respectively. In the discrete case, i.e. with the surface S in terms of a shape model, the integral in Eq. (1) as well as its derivatives with respect to the Cartesian coordinates can also be found in Werner & Scheeres (1996). Equation (1) according to Werner & Scheeres (1996) was used for computing the gravitational potential on the outer spheroid that entered a subsequent harmonic analysis. The input to the analysis is shown in Figure 4 for Bennu and in Figure 5 for Castalia.

4.2. Harmonic analysis on the spheroid

The solution to the exterior Dirichlet problem for the spheroid provides the gravitational potential $V(u, \vartheta, \lambda) = V$ as (Lebedev, 1972, p.218)

$$V = \frac{GM}{\sqrt{u_0^2 + E^2}} \sum_{n=0}^{\infty} \sum_{m=0}^{n} \frac{Q_{n,m}(\eta)}{Q_{n,m}(\eta_0)} \left(\bar{C}^e_{n,m} \cos m\lambda + \bar{S}^e_{n,m} \sin m\lambda \right) \bar{P}_{n,m} \tag{2}$$

where $\bar{C}^e_{n,m}, \bar{S}^e_{n,m}$ denote the cosine and sine harmonic coefficients of degree n and order m, GM stands for the planetocentric (here the asteroid-centric) gravitational constant, u is the semi-axis of the reference spheroid according to Figure 3,

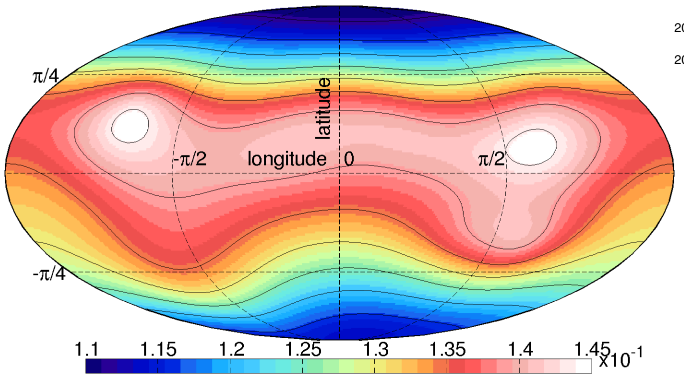

Figure 5: Gravitational potential on the outer spheroid for Castalia computed with Eq. (1) – the input signal to the harmonic analysis (in m^2s^{-2}).

$\bar{P}_{n,m} = \bar{P}_{n,m}(\cos\vartheta)$ and $Q_{n,m}$ is the associated Legendre function of the first and the second kind, respectively. The angle ϑ is sometimes called the reduced co-latitude (the polar angle of a bounding sphere). Note the bar in Legendre function $\bar{P}_{n,m}$ denotes the normalization that keeps its values in the numerical range of the computer; e.g., see Press (2007, p.294). The term $Q_{n,m}(\eta_0)$ in Eq. (2) is somewhat arbitrary but it follows the convention adopted by Hobson (1931, p.417). The arguments η_0 and η share the same value for the linear eccentricity $E^2 = a^2 - u_0^2 = a^2 - u^2$ so that the spheroids u and u_0 are confocal. The prolate and oblate spheroidal harmonics differ in the argument η. For the oblate case it holds $\eta = \frac{iu}{E}$ (with i the imaginary unit), while it is $\eta = \frac{\sqrt{u^2+E^2}}{E}$ in the prolate case. The definition of $Q_{n,m}$ and the relevant computational schemes are subject of Appendix A. Generally, the series in Eq. (2) sums up to infinity and a set of harmonic coefficients limited by a certain integer $N_{\max}$ is usually called the gravitational (or gravity) field model.

Once we work with the (u, ϑ, λ) domain, in which the Laplace's equation is separable, the harmonic coefficients can be obtained by the spheroidal harmonic analysis

$$\begin{matrix}\bar{C}^e_{n,m} \\ \bar{S}^e_{n,m}\end{matrix} = \frac{\sqrt{u_0^2+E^2}}{GM}\frac{Q_{n,m}(\eta_0)}{Q_{n,m}(\eta)}\iint_\sigma V(\vartheta,\lambda)\begin{matrix}\cos m\lambda \\ \sin m\lambda\end{matrix}\bar{P}_{n,m}(\vartheta)\,\mathrm{d}\sigma, \tag{3}$$

where we integrate the potential over a spheroid with dσ referring to the surface σ indicated in Figure 3 by the dashed line (the surface σ is the bounding sphere; see Lowes & Winch, 2012, p. 6). Equation (3) presents nothing else than the spherical harmonic analysis from Press (2007, p. 296) adapted for the spheroidal coordinates and multiplied by $Q_{n,m}$ functions (Lowes & Winch, 2012).

The bounding spheroids depicted in Figures 1, 2 associated with η present our choice for the so-called Brillouin surface (or the outer Runge surface, see Freeden & Gerhards, 2012, p. 25), below which the outer harmonic coefficients do not converge (Takahashi & Scheeres, 2014). These spheroids are by their whole surface above all masses so that Eq. (1) can be used for expressing the outer gravitational potential. Note that the equivalent spherical Brillouin surface would be farther from the asteroid at the poles for the oblate body, and at the equator for the prolate body, respectively.

Note that Eq. (1) may also serve as a starting point for computing various partial derivatives of the potential from a shape model (Werner & Scheeres, 1996). In this case (a grid-wise approach followed by the quadrature), the harmonic analysis must be accommodated accordingly. Among many partial derivatives of V, the most suitable input quantities seem to be the derivatives with respect to u (i.e., V_u, V_{uu} etc.). This is because only the $Q_{n,m}$ functions in front of the integration symbol need to be differentiated; e.g., Eq. (3) for V_u reads

$$\begin{matrix}\bar{C}^e_{n,m} \\ \bar{S}^e_{n,m}\end{matrix} = \frac{\sqrt{u_0^2+E^2}}{GM}\frac{Q_{n,m}(\eta_0)}{\partial Q_{n,m}(\eta)/\partial u}\iint_\sigma V_u(\vartheta,\lambda)\begin{matrix}\cos m\lambda \\ \sin m\lambda\end{matrix}\bar{P}_{n,m}(\vartheta)\,\mathrm{d}\sigma. \tag{4}$$

5. Choice of the spheroid parameters

Parameters of the biaxial encompassing spheroids shown in Figure 1 and 2 were found by the following procedure. First, we found the semi-axes a'_0, b'_0, c'_0 of the triaxial ellipsoid that best fits the shape model. This was done by least-squares fitting of the quadratic surface in terms of its general form (Rektorys, 1994)

$$\sum_{i=1}^{3}\sum_{j=1}^{3} p_{ij}\zeta_i\zeta_j + 2\sum_{i=1}^{3} r_i\zeta_i = 1 \tag{5}$$

where the parameters p_{ij}, r_i define the quadratic surface and $\zeta \in \{x, y, z\}$. Because the coordinate axes and the origin of Bennu and Castalia shape models coincide with principal axes (Nolan et al., 2013; Hudson & Ostro, 1994), we can use a simplified form of Eq. (5) (Andrews & Séquin, 2014)

$$p_{11}x_1^2 + p_{22}x_2^2 + p_{33}x_3^2 = 1, \tag{6}$$

where the mixed and linear terms responsible for the rotation and translation are avoided.

Then, the semi-axes a'_0, b'_0, c'_0 of the triaxial ellipsoid can be obtained from the eigenvalue problem $\left[\mathbf{A}(p_{ij}) - \mathbf{D}\right]\mathbf{V} = 0$, where $\mathbf{D} = \lambda\mathbf{I}$ and $\mathbf{V}$ contain the eigenvalues and the eigenvectors, respectively (with $\mathbf{I}$ the identity matrix). The semi-axes are then (Ruiz et al., 2013)

$$\begin{pmatrix} a_0'^{-2} & 0 & 0 \\ 0 & b_0'^{-2} & 0 \\ 0 & 0 & c_0'^{-2}\end{pmatrix} = \mathbf{D}. \tag{7}$$

We have checked the results from Eq. (6) with those from Eq. (5) with differences of a few centimetres (relative agreement 10^{-5}).

In order to get the parameters a_0, b_0 of the spheroid, the two closest values from a'_0, b'_0, c'_0 have been averaged. The spheroid a_0, b_0 is chosen to be a reference spheroid that intersects the shape model and that is indicated by η_0 in Eq. (2). With a fixed value of numerical eccentricity $E^2 = |a_0^2 - b_0^2|$ the semi-axes of the outer (bounding) confocal spheroid were found by looking

Table 2: Parameters of the spheroids used in this study. Note the magnitude of a_0' corresponds with b and u for Castalia because the x, y, z were rotated for 90° about the y−axis; then a new z−axis is the spheroid's axis of rotational symmetry according to Figure 3. For Bennu $E_B^2 = 1.1308 \cdot 10^4$ m^2 while it is $E_C^2 = 6.0987 \cdot 10^5$ m^2 for Castalia. The semiaxes are given in meter, the density in kg $\cdot$ m^{-3}.

Name	Density	$a_0'/b_0'/c_0'$	a/b	a_u/u
Bennu	2100	259/250/231	254/231	$(u^2 + E_B^2)^{\frac{1}{2}}/271$
Castalia	1260	901/480/420	450/901	$974/(a_u^2 - E_C^2)^{\frac{1}{2}}$

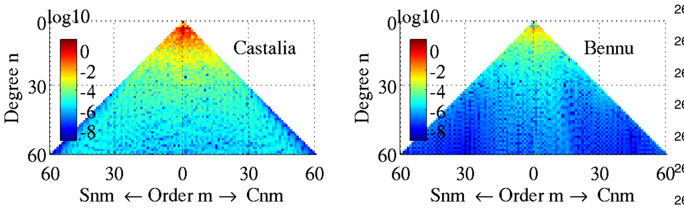

Figure 6: Spectra of the spheroidal gravity field models of Bennu and Castalia.

for a point P of the shape model that has a maximum value of the semi-axis b_P. Finally, any choice $u > b_P$ with fixed E^2 may define an outer confocal spheroid with respect to the reference spheroid. The outer spheroids for both bodies are depicted in Figure 1 and 2 and Table 2 provides their numerical parameters.

6. Results – harmonic models of the exterior gravity field

In order to obtain spheroidal coefficients, the spheroidal harmonic analysis was applied to a grid with the gravitational potential calculated with Eq. (1) and shown in Figures 4, 5. A choice of the maximum degree of the harmonic series is customary but it should be chosen with care to capture a high-frequency signal. In general, these high frequencies may come both from the density/mass anomalies (not possible here due to the assumption of the constant density) inside the body and from the shape model. The latter issue is pointed out in Takahashi & Scheeres (2014, p.172) by stating that "The polyhedral gravity field ... contains information of infinitely higher-degree and higher-order expansion". This is caused by the discretization in terms of triangular facets producing high frequencies. Hence, to reduce or to look at the effect of these high frequencies on low-degree coefficients, the harmonic analysis can be performed up to higher spheroidal harmonic degrees and orders (more in Sec. 6.1.1).

The final harmonic analysis was applied to the Gauss-Legendre grid up to degree and order 360 of a dimension 361 × 720 points (see Sec. 6.1.1). This kind of grid is sampled at latitudes with $P_n(\vartheta) = 0$ and it leads to the Gauss-Legendre quadrature (Press, 2007). The precision of the harmonic analysis was checked by the backward computation of the potential from the obtained coefficients. For both bodies we obtained a relative accuracy of 10^{-7} that means the original and the computed potential have minimally seven common digits (with RMS about 9–10 digits). The coefficients up to degree 60 are displayed in Figure 6. We can see that the power of the coefficients dramatically decreases with increasing degree, especially for Bennu due to its simpler shape.

Note the maximum degree 360 does not necessarily mean that a physically meaningful signal will be present over such high frequencies. Here the degree of 360 increased the number of common digits in the backward test by reducing the aliasing. Nevertheless, the question what degrees or individual coefficients can be neglected (if any) may be important in the applications such as geophysical exploration or navigation of the explorers in the body's neighbourhood (e.g., for the mission OSIRIX-REx). Besides the accuracy of the coefficients, the role of high-degree coefficients depends not only on the distance from the body but also on the function computed with these coefficients. In particular, the partial derivatives of the potential may be important for detailed geophysical exploration with gravity data, whereas these derivatives are usually more sensitive to higher frequencies than the potential[3]. In Appendix Appendix B, the gradient components and the second-order derivatives for both bodies are shown; to download these data visit http://galaxy.asu.cas.cz/planets/index.php?page=sgfm.

6.1. Discussion of error sources

Our solutions may be affected by the errors of different nature. The most obvious imperfection comes from the assumption of the constant density. The obtained harmonic models are fully subject of this methodological constraint and they should be used with this in mind. This issue can only be investigated with independent gravity data sets if available, e.g. with fly-by orbits or with information on the rotational state of the asteroid.

Besides the uncertainty of the shape model (see Sections 2, 3), another imperfection origins from the inaccuracy of the density ρ used in Eq. (1). For Bennu it is 1260±70 kg/m^3 while for Castalia it is 2100±400 kg/m^3 (Scheeres et al., 1996). However, from Eq. (1) we can see this error linearly affects the gravitational potential. This means the obtained harmonic coefficients can eventually be re-scaled if some more accurate estimate of ρ is known. For example, the fraction $\rho_{\mathrm{new}}/\rho_{\mathrm{old}}$, where ρ_{old} is the density used in the integration, adjusts the harmonic coefficients to a new value ρ_{new}. The uncertainty of the bulk density (which is assumed to be constant) is directly linked with the uncertainty of the bulk porosity as these two are related by $P = 1 - \rho/\rho_{\mathrm{M}}$, where ρ_{M} is the appropriate meteorite analog density. This relation can be disentangled only with two independent information; e.g., from a shape model from radar measurements and from the fly-by orbit perturbations.

6.1.1. Aliasing and discretization

Furthermore, the harmonic coefficients may be affected by aliasing due to a high-frequency signal that may come either from the integration of a discrete shape model and the

[3]For example, for the Earth the mission GOCE (Drinkwater et al., 2003) has acquired second-order derivatives to reveal more information on the Earth's gravitational field from a satellite altitude, whereas the same maximum degree could hardly be obtained with the potential or its gradient observed at the same altitude.

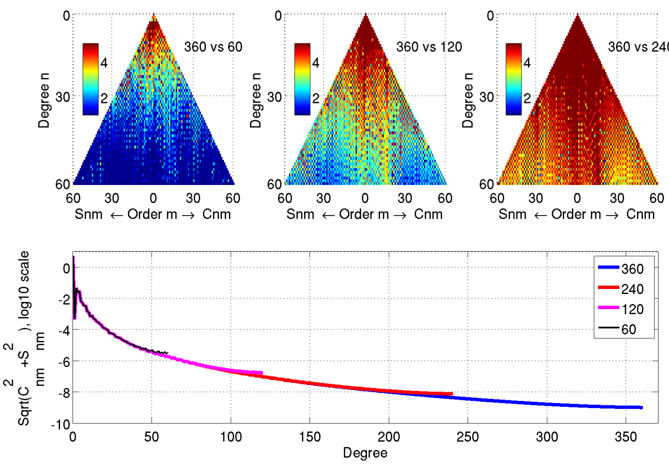

Figure 7: Bennu: effect of aliasing in terms of common decimal digits (top panels) and the corresponding power spectra.

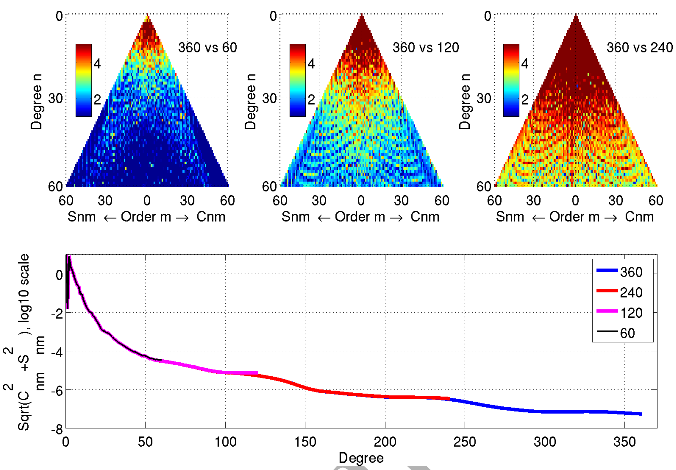

Figure 8: Castalia: effect of aliasing in terms of common decimal digits (top panels) and the corresponding power spectra.

use of spheroidal harmonics for approximating its gravitational potential (see Takahashi & Scheeres, 2014, p.172), or from mass/density anomalies not considered in the modelling (a richer signal than assumed). As the density is assumed to be constant, we face only the aliasing caused by the first issue. In order to study this type of aliasing, we have applied the harmonic analysis to multiple grids with varying spatial resolution, whereas increasing the grid resolution increases the accuracy of the obtained harmonic coefficients.

The maximum degree is linked with a grid dimension since we employ the Gauss-Legendre quadrature for the harmonic analysis by Eq. (3). For this quadrature we can obtain degree N if the grid has a dimension $(N+1) \times 2N$. In particular, we have used dimensions $61 \times 120, 121 \times 240, 241 \times 480, 361 \times 720$ that have yielded harmonic coefficients up to the degree 60, 120, 240, 360.

For degree 360 we obtained the best agreement with the input potential and the potential computed from the coefficients. In Figure 7 and 8 the problem is documented in terms of common digits in the harmonic coefficients (top panels). We compare the solution up to degree and order 360 with all other solutions within the first 60 degrees. It is clear that the number of common digits increases up to more than 5 digits if the maximum degree increases too. Furthermore, the effect of aliasing is also seen in the square root of power spectra (bottom panels) as the solutions to degrees 60, 120 and 240 depart from the solution to degree 360 near these degrees. For this reason, we take the final harmonic coefficients from the solution up to degree 360. Note that this maximum degree does not necessarily mean that such high degrees are physically meaningful. We recommend to use such coefficients that, in agreement with power spectra in Figure 7 and 8, provide magnitudes small enough to be neglected in a particular application (say < 100).

6.2. *Signal near the Brillouin spheroid*

Although the obtained spheroidal models represent the exterior gravitational field with respect to the spheroid, onto which the harmonic analysis was performed, the models can formally

Table 3: Differences in percent between Eq. (1) and Eq. (2) near the Brillouin spheroid. The table complements Figures 9 and 10, whereas the distance is measured along the normal from a triangular facet and the symbol "s" for Bennu denotes that the spherical coefficients were used. Note that the same maximum degree for the spheroidal and spherical series does not automatically provide the same spectral content.

Distance (meters)/Degree	Min	Max	RMS
Bennu			
5/20	10^{-4}	3.2	0.85
5/60	10^{-4}	6.3	1.0
30/60	10^{-5}	1.8	0.58
5/20 (s)	10^{-4}	3.3	0.86
5/60 (s)	10^{-4}	68	4.1
5/100 (s)	10^{-3}	>100	>100
Castalia			
5/20	4.3	22	12
5/60	4.3	22	12
100/60	10^{-3}	14	5.4

be used in the space under the Brillouin spheroid but above the shape model. Inside the Brillouin spheroid, the spheroidal harmonics generally do not converge (Takahashi & Scheeres, 2014) so special care must be taken to the choice of the maximum degree. High degrees may dramatically distort the computed signal under the Brillouin spheroid.

In Figure 9 we demonstrate the difference between the potential computed with the spheroidal models and that computed from Eq. (1) near the Brillouin spheroid. The black dots indicate the points above the Brillouin spheroid, while the distance from the shape model is measured along the normal to a triangular facet. The total distance along this normal to the spheroid is shown in the bottom panels of Figure 9 for each triangular facet. For both bodies we can see that the differences decrease with increasing distance from the body. As seen from Table 3, associated maxima and RMS values are much smaller for Bennu

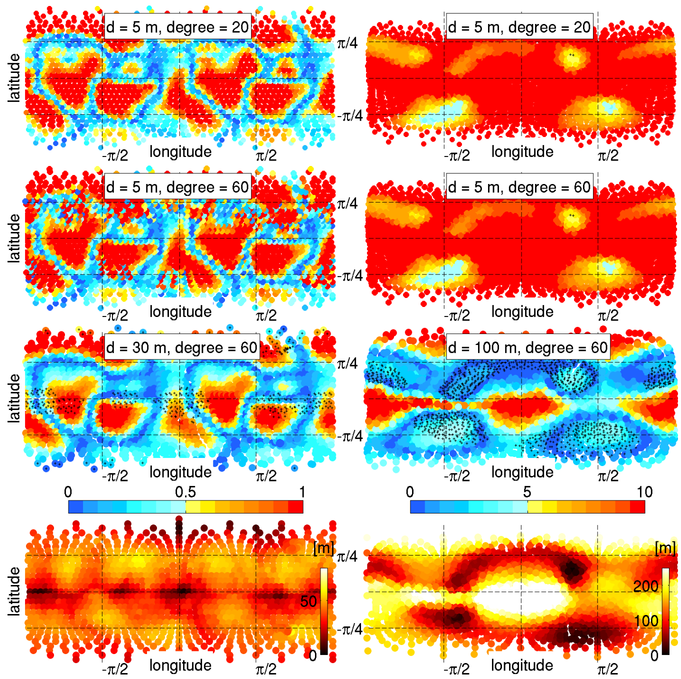

Figure 9: Differences in percent between Eq. (1) and Eq. (2) near the Brillouin spheroid with Bennu in the left and Castalia in the right panels. The black dots indicate points above the Brillouin spheroid, whereas the distance is measured along the normal to each triangle of the shape model. The distance along this normal to the spheroid is shown in two bottom panels.

as the spheroidal approximation better suits to its shape; compare Figures 1 and 2. The shape of Castalia seems to be more complex and the spheroidal harmonics seem to provide a worse service for representing the gravitational field. For Bennu we have 1% difference in RMS in the potential 5 m above its surface, while we have about 12% in RMS for Castalia and the same distance. In case of Bennu, such a detailed gravitational field model may be of special interest since the OSIRIX-REx mission is planned to reach this asteroid in 2018 (Drake et al., 2011).

6.3. Spherical harmonic model for Bennu

Regarding a relatively regular shape of Bennu and a possible need for accurate navigation of the OSIRIS-REx satellite, which will likely prefer spherical than spheroidal harmonics, we have also transformed Bennu's spheroidal coefficients into the spherical coefficients by the Hotine-Jekeli's transformation defined in Hotine (1969); Jekeli (1988). The resulting coefficients are also provided at http://galaxy.asu.cas.cz/planets/index.php?page=sgfm.

The practical advantage of the spherical harmonics is their wide use across the disciplines so that a lot of existing software can employ them. Note the more irregular shape of the body (e.g., Castalia) the less suitable may be the spherical harmonics for modelling its gravitational field with one set of coefficients, e.g., see Takahashi & Scheeres (2014).

The spherical harmonics can also be used inside the Brioullin surfaces if the series is reasonably truncated as in Figure 9 for the spheroidal harmonics to degree 60. This behaviour is shown

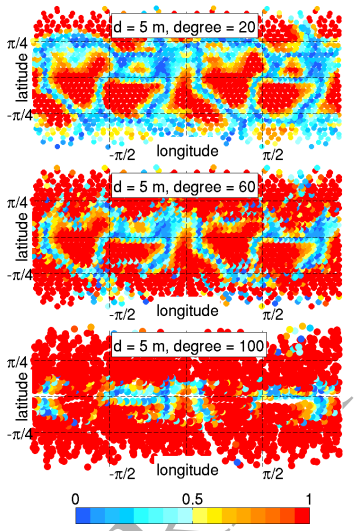

Figure 10: Bennu: Degree dependence of the differences under the Brioullin spheroid (in percent) between Eq. (1) and the potential computed with the spherical coefficients obtained from the Hotine-Jekeli's transformation. Compare with two upper left panels of Figure 9 where the same distance from the body is used. Note the spherical harmonic degree 60 does not correspond with the spheroidal harmonic degree 60 exactly; the same signal generates different bandwidths in spheroidal and spherical harmonics.

in Figure 10, where the agreement of Eq. 1 with spherical harmonics is plotted as a function of the maximum degree (20, 60 and 100) 5 metres above each triangular facet. Figure 10 is to be compared with the two upper left panels of Figure 9, where the same distance (5 m) from Bennu is considered. Although degree 60 in spherical harmonics is not the same as this degree in spheroidal harmonics, we can observe that both panels provide good agreement so that even the spherical coefficients can be used near Bennu's surface. Although not significantly, Table 3 indicates why spheroidal harmonics may provide a better service than the spherical harmonics in close proximity to the body. The same degree 60 produces four times worse agreement with Eq. (1) in terms of RMS so that spheroidal harmonics, depending on the u and a_u, may capture more signal with less coefficients and may less deviate from a true field up to a certain degree. Finally, spherical harmonic degree 100 in Figure 10 demonstrates we can expect much worse agreement for higher spherical degrees near the Bennu's surface.

7. Summary

A use of the spheroidal harmonics to express the exterior gravitational field of a small and constant-density body with a given shape (polyhedral) model is studied.

In general, the spheroidal harmonics offer interesting biaxial flexibility when modelling the gravitational field of (not only) a small body. First, they can account for more irregular shape than the spherical harmonics while the Brillouin surface can be very close to an oblate or prolate body. Secondly, they can easily be evaluated up to very high degrees that may help to control the effects from aliasing and/or high-frequency noise in the data. In addition, the harmonic representations can easily be filtered in the spectral domain, which may support geophysical interpretation over a specific bandwidth and region of interest. For example, a low-degree expansion derived from orbit perturbations, which usually provide information on the true gravitational field, may constrain a high-degree expansion derived from the shape model to test the constant-density hypothesis, to identify mascon-like objects, etc.

In this contribution, we have obtained spheroidal harmonic models of the gravitational field of (101955) Bennu and (4769) Castalia by the grid-wise spheroidal harmonic analysis. The spheroidal model for Bennu is accompanied with the spherical model obtained by the spheroidal-to-spherical transformation. As seen from Figures 9, 10 and Table 3 for Bennu, there is nearly identical agreement of the spheroidal and spherical harmonics up to degree 20 about 5 metres above the surface. For degree 60 and this altitude, however, we can see that the spheroidal harmonics perform slightly better than the spherical harmonics (1% vs. 4% agreement in RMS). With increasing distance from a body, in turn, the role of either type of harmonics can be expected less significant. Hence, in a real application, the data quality and a particular purpose will best constrain the choice of the basis functions. Along with harmonic models we provide the first and the second-order derivatives of the potential situated on the outer spheroid in the local South-East-Up frame (see Appendix B). All the data can be found at http://galaxy.asu.cas.cz/planets/index.php?page=sgfm.

When converting a gravitational field of the shape models into the harmonic representation it was crucial to mitigate the effect of aliasing arising from the point-wise integration with Eq. (1). This was achieved by increasing the spheroidal harmonic degree of the series up to degree 360 as illustrated by Figures 7, 8 in terms of common digits in the coefficients. By the backward computation of the gravitational potential from these coefficients, we have obtained 9-10 common digits in terms of RMS.

The procedure described here is fully deterministic so that all solutions and other outputs depend on "outer" factors, which need to be taken into account before the application. The most important are i) the accuracy of the density of the body in question, ii) the assumption that the density is constant, and iii) the accuracy of the shape model. While the obtained coefficients can easily be scaled to satisfy another value of the density, the harmonic coefficients must be determined again if a new and more accurate shape model becomes available.

Acknowledgments

The work was supported by the projects RVO:67985815 and LH13071. We thank two anonymous reviewers for their careful reading and useful suggestions.

Appendix A. Computing Legendre functions of the second kind via hypergeometric formulation

In this paper, we compute the associated the Legendre functions of the second kind (ALFs) by means of the hypergeometric formulation with modifications described in this section. From Abramowitz et al. (1965, Eq. 8.1.3) we have

$$Q_{n,m}(\eta) := (-1)^m \frac{\sqrt{\pi}(n+m)!}{2^{n+1}(n+1/2)!} \frac{\left(\eta^2-1\right)^{\frac{m}{2}}}{\eta^{n+m+1}} \times {}_2F_1\left(\frac{n+m+2}{2}, \frac{n+m+1}{2}, n+\frac{3}{2}, \frac{1}{\eta^2}\right), \tag{A.1}$$

where $\eta = i\frac{u}{E}$ and $\eta = \frac{\sqrt{u^2+E^2}}{E}$ is for the oblate and prolate spheroid, respectively. The Gauss hypergeometric function is defined as (Abramowitz et al., 1965, p. 556):

$$ {}_2F_1(\alpha,\beta,\gamma,\delta) = \sum_{k=0}^{\infty} \frac{(\alpha)_k(\beta)_k}{(\gamma)_k} \frac{\delta^k}{k!}, \tag{A.2}$$

where $(x)_k = \frac{\Gamma(x+k)}{\Gamma(x)} = \frac{(x+k-1)!}{(x-1)!}$ is the Pochhammer symbol, Γ is the Gamma function and k the integer index of the hypergeometric series. The series is to be summed to a maximum $k_{\max}$ guaranteeing a numerical convergence. The speed of the convergence can be accelerated by a transformation of the hypergeometric formulation, which would change the relative size of α, β, γ and δ (e.g., decreasing δ etc.).

Note the series in Eq. (A.2) may contain both the positive and negative terms so that its evaluation may also face the cancellation. To accelerate the summation and to avoid the cancellation, we chose a different transformation of ${}_2F_1$ for the oblate and prolate cases.

Appendix A.1. Oblate ALFs

For the oblate case we employ the transformation

$$ {}_2F_1(\alpha',\beta',\gamma',\delta') = (1-\delta)^{-\beta}\, {}_2F_1\left(\beta, \gamma-\alpha, \gamma, \frac{\delta}{\delta-1}\right), \tag{A.3}$$

which for Eq. (A.1) gives

$$Q_{n,m}(\eta) = (-1)^{\frac{2m+n+1}{2}} \frac{\sqrt{\pi}(n+m)!}{2^{n+1}(n+1/2)!} \left(\eta^2-1\right)^{-\frac{n+1}{2}} \times {}_2F_1\left(\frac{n+m+1}{2}, \frac{n-m+1}{2}, n+\frac{3}{2}, \frac{1}{1-\eta^2}\right). \tag{A.4}$$

and then, by back substitution $\eta = \frac{iu}{E}$, we obtain

$$Q_{n,m}\left(\frac{iu}{E}\right) = (-1)^m \frac{\sqrt{\pi}(n+m)!}{2^{n+1}(n+1/2)!} \left(\frac{E}{\sqrt{u^2+E^2}}\right)^{n+1} \times {}_2F_1\left(\frac{n+m+1}{2}, \frac{n-m+1}{2}, n+\frac{3}{2}, \frac{E^2}{u^2+E^2}\right). \tag{A.5}$$

Appendix A.2. Prolate ALFs

For the prolate case we employ a different transformation

$$ {}_2F_1(\alpha',\beta',\gamma',\delta') = (1-\delta)^{\gamma-\alpha-\beta}\, {}_2F_1\left(\gamma-\alpha, \gamma-\beta, \gamma, \delta\right), \tag{A.6}$$

which again with Eq. (A.1) gives

$$\begin{aligned}Q_{n,m}(\eta) =&(-1)^m \frac{\sqrt{\pi}(n+m)!}{2^{n+1}(n+1/2)!}\frac{\left(\eta^2-1\right)^{-\frac{m}{2}}}{\eta^{n-m+1}}\\ &\times {}_2F_1\left(\frac{n-m+1}{2},\frac{n-m+2}{2},n+\frac{3}{2},\frac{1}{\eta^2}\right).\end{aligned} \tag{A.7}$$

and by back substitution $\eta = \frac{\sqrt{u^2+E^2}}{E}$ it yields

$$\begin{aligned}Q_{n,m}\left(\frac{a_u}{E}\right) =&(-1)^m \frac{\sqrt{\pi}(n+m)!}{2^{n+1}(n+1/2)!}\left(\frac{E}{u}\right)^m\left(\frac{E}{\sqrt{u^2+E^2}}\right)^{n-m+1}\\ &\times {}_2F_1\left(\frac{n-m+1}{2},\frac{n-m+2}{2},n+\frac{3}{2},\frac{E^2}{u^2+E^2}\right).\end{aligned} \tag{A.8}$$

Appendix A.3. Derivatives of Q_{nm} and the summing scheme

Eqs. (A.5) and (A.8) for the zeroth-order derivatives of $Q_{n,m}$ with respect to u can be rewritten as a multiplication of the hypergeometric series and the function of u, degree and order.

$$Q^0_{n,m}(u) = \beta_{n,m}(u)\sum_{k=0}^{\infty}\alpha_{n,m,k}(u), \tag{A.9}$$

where the superscript denotes the order of differentiation with respect to u. From this recipe one obtains summing schemes for the first $Q^1_{nm} = \frac{\partial Q_{nm}}{\partial u}$ and the second derivative $Q^2_{nm} = \frac{\partial^2 Q_{nm}}{\partial u^2}$ as follows

$$\begin{aligned}Q^1_{n,m}(u) &= \frac{\partial \beta_{n,m}}{\partial u}\sum_{k=0}^{\infty}\alpha_{n,m,k} + \beta_{n,m}\sum_{k=0}^{\infty}\frac{\partial \alpha_{n,m,k}}{\partial u},\\ Q^2_{n,m}(u) &= \frac{\partial^2 \beta_{n,m}}{\partial u^2}\sum_{k=0}^{\infty}\alpha_{n,m,k} + 2\frac{\partial \beta_{n,m}}{\partial u}\sum_{k=0}^{\infty}\frac{\partial \alpha_{n,m,k}}{\partial u} + \beta_{n,m}\sum_{k=0}^{\infty}\frac{\partial^2 \alpha_{n,m,k}}{\partial u^2}.\end{aligned}$$

The starting value is $\alpha_{n,m,0} = 1$ while $\beta_{n,m}$ functions are to be obtained from Eqs. (A.5), (A.8).

Appendix A.4. Checking $Q^0_{nm}, Q^1_{nm}, Q^2_{nm}$

There are multiple possibilities how to check the computation of the ALFs of the second kind. Here, we make use of the Legendre differential equation, which allows to verify partial derivatives of $Q_{n,m}$ up to the second order at the same time. We proceed from Lebedev (1972, Eqs. 8.6.7 and 8.6.13), where we set $\sinh\alpha = \frac{u}{E}$ and $\cosh\alpha = \frac{\sqrt{u^2+E^2}}{E}$. Then the LDE in terms of u for oblate functions reads

$$(u^2+E^2)\frac{\partial^2 Q_{nm}}{\partial u^2} + 2u\frac{\partial Q_{nm}}{\partial u} - \left[n(n+1) - \frac{m^2E^2}{u^2+E^2}\right]Q_{nm} = 0 \tag{A.10}$$

and similarly for the prolate functions we get

$$(u^2+E^2)\frac{\partial^2 Q_{nm}}{\partial u^2} + \frac{2u^2+E^2}{u}\frac{\partial Q_{nm}}{\partial u} - \left[n(n+1) + \frac{m^2E^2}{u^2}\right]Q_{nm} = 0. \tag{A.11}$$

From the Legendre differential equation and Eq. (A.1) we see that Q_{nm} can be multiplied by an appropriate degree-order function that may cancel out some cumbersome terms in Eq. (A.1). For example, we can introduce the normalization $\bar{Q}_{n,m} = H_{n,m}Q_{n,m}$, where $H_{n,m} = (-1)^m\frac{2^{n+1}(n+1/2)!}{\sqrt{\pi}(n+m)!}$. With such or similar normalization one can better control the behaviour in high degrees and orders.

Appendix B. Cartesian derivatives of the gravitational potential in the local frame

The Cartesian derivatives of the potential in spheroidal harmonics can be derived from ordinary partial derivatives of Eq. (2) by using the algorithm described in Koop (1993); Casotto & Fantino (2009). The algorithm starts with the coordinates from Table 1 and the associated covariant metric g_{ij}. Here, we provide relations specifically for the second-order derivatives as they are rarely or not at all present in the literature. Figures B.11 and B.12 show their numerical values on the outer spheroid. In both figures we sum from degree 5 to illustrate the short-wavelength signal. The Cartesian derivatives in the local South-East-Up (x', y', z') frame for the oblate spheroid are defined (compare with Koop, 1993, p.31)

$$\begin{aligned}V_{x'} &= \frac{1}{L}V_\vartheta,\ V_{y'} = \frac{1}{v\sin\vartheta}V_\lambda,\ V_{z'} = \frac{v}{L}V_u\\ V_{x'x'} &= \frac{uv^2}{L^4}V_u + \frac{1}{L^2}V_{\vartheta\vartheta} + \frac{E^2\cos\vartheta\sin\vartheta}{L^4}V_\vartheta\\ V_{x'y'} &= \frac{1}{vL\sin\vartheta}V_{\vartheta\lambda} - \frac{\cot\vartheta}{vL\sin\vartheta}V_\lambda\\ V_{x'z'} &= \frac{uv}{L^4}V_\vartheta - \frac{v}{L^2}V_{u\vartheta} - \frac{vE^2\cos\vartheta\sin\vartheta}{L^4}V_u\\ V_{y'y'} &= \frac{u}{L^2}V_u + \frac{1}{v^2\sin^2\vartheta}V_{\lambda\lambda} + \frac{\cot\vartheta}{L^2}V_\vartheta\\ V_{y'z'} &= \frac{u}{Lv^2\sin\vartheta}V_\lambda + \frac{1}{L\sin\vartheta}V_{u\lambda}\\ V_{z'z'} &= \frac{v^2}{L^2}V_{uu} - \frac{uE^2\sin^2\vartheta}{L^4}V_u - \frac{E^2\cos\vartheta\sin\vartheta}{L^4}V_\vartheta\end{aligned}$$

where $v = \sqrt{u^2+E^2}$ and $L = \sqrt{u^2+E^2\cos^2\theta}$.

For the prolate spheroid we obtain similar relations

$$\begin{aligned}V_{x'} &= \frac{1}{L}V_\vartheta,\ V_{y'} = \frac{1}{u\sin\vartheta}V_\lambda,\ V_{z'} = \frac{v}{L}V_u\\ V_{x'x'} &= \frac{uv^2}{L^4}V_u + \frac{1}{L^2}V_{\vartheta\vartheta} - \frac{E^2\cos\vartheta\sin\vartheta}{L^4}V_\vartheta\\ V_{x'y'} &= \frac{1}{uL\sin\vartheta}V_{\vartheta\lambda} - \frac{\cot\vartheta}{uL\sin\vartheta}V_\lambda\\ V_{x'z'} &= -\frac{uv}{L^4}V_\vartheta + \frac{v}{L^2}V_{u\vartheta} - \frac{vE^2\cos\vartheta\sin\vartheta}{L^4}V_u\\ V_{y'y'} &= \frac{v^2}{uL^2}V_u + \frac{1}{u^2\sin^2\vartheta}V_{\lambda\lambda} + \frac{\cot\vartheta}{L^2}V_\vartheta\\ V_{y'z'} &= -\frac{v}{u^2L\sin\vartheta}V_\lambda + \frac{v}{uL\sin\vartheta}V_{u\lambda}\\ V_{z'z'} &= \frac{v^2}{L^2}V_{uu} - \frac{uE^2\cos^2\vartheta}{L^4}V_u + \frac{E^2\cos\vartheta\sin\vartheta}{L^4}V_\vartheta\end{aligned}$$

where it holds $v = \sqrt{u^2+E^2}$ and $L = \sqrt{u^2+E^2\sin^2\theta}$.

References

Abramowitz, M., Stegun, I. A. et al. (1965). *Handbook of mathematical functions* volume 1046. Dover New York.

Andrews, J., & Séquin, C. H. (2014). Type-constrained direct fitting of quadric surfaces. *Computer-Aided Design and Applications*, *11*, 107–119.

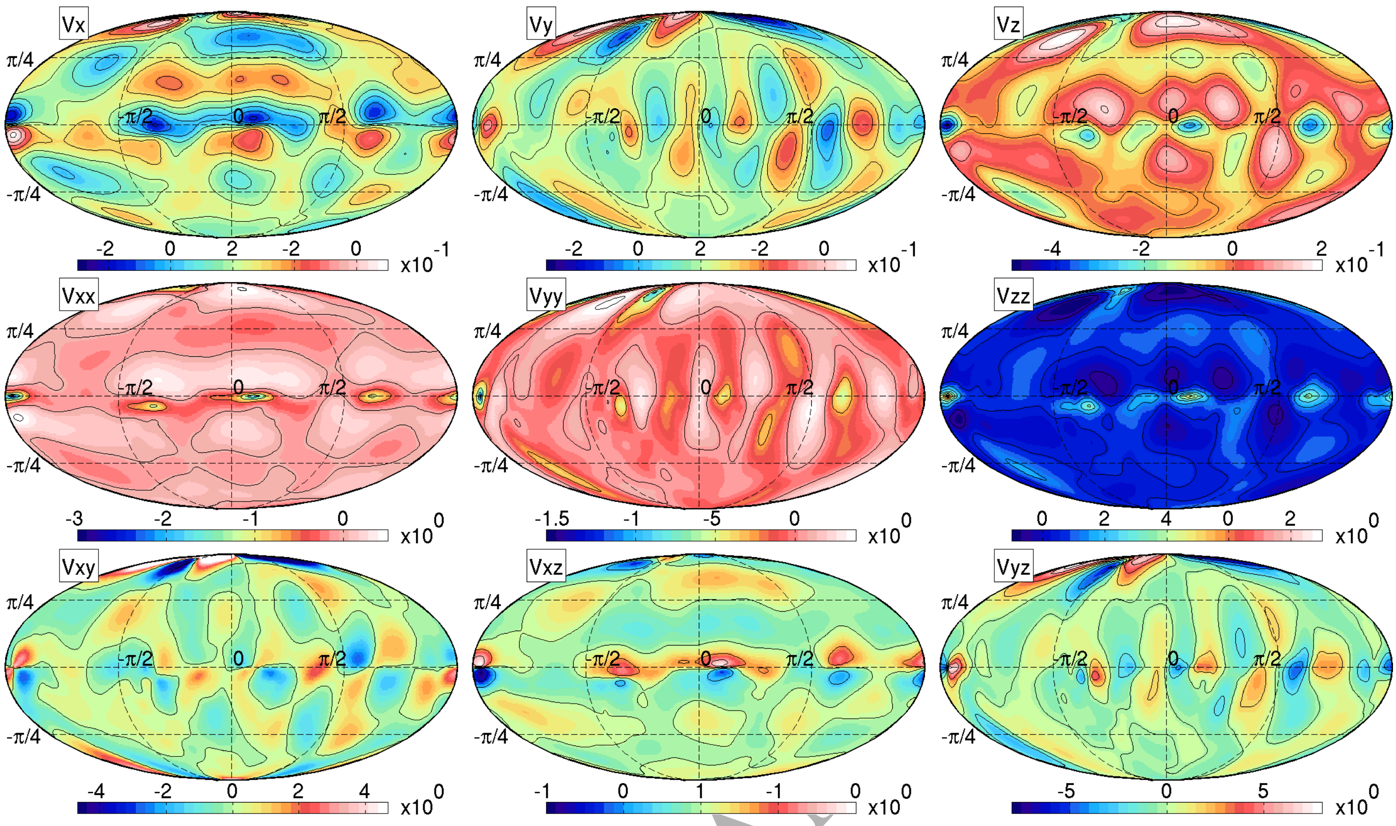

Figure B.11: Bennu: the first (in mGal) and second-order Cartesian derivatives (in eotvos = 10^{-9} s^{-2}) of the potential from the degree 5.

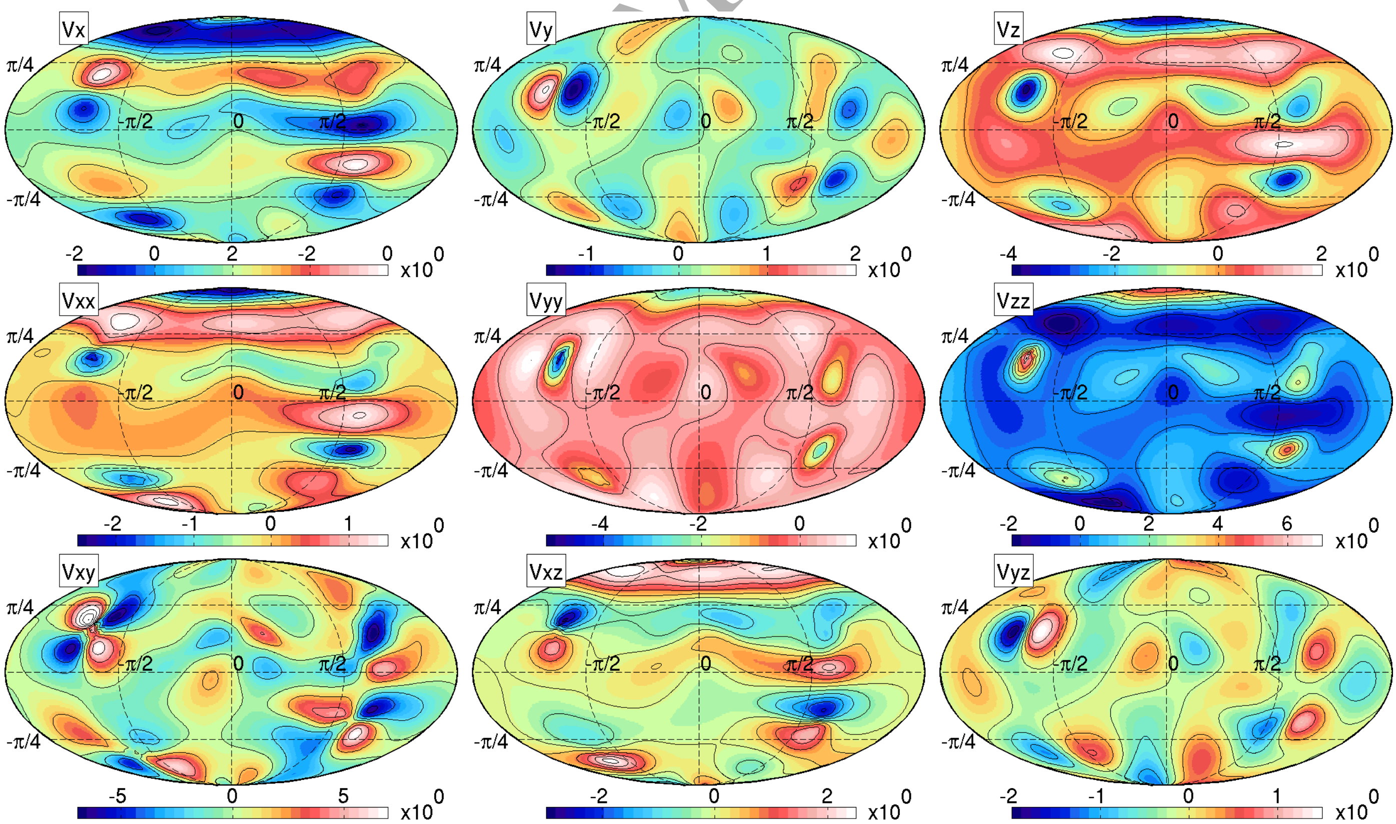

Figure B.12: Castalia: the first (in mGal) and second-order Cartesian derivatives (in eotvos = 10^{-9} s^{-2}) of the potential from the degree 5.

Balmino, G. (1994). Gravitational potential harmonics from the shape of an homogeneous body. *Celestial Mechanics and Dynamical Astronomy*, *60*, 331–364.

Casotto, S., & Fantino, E. (2009). Gravitational gradients by tensor analysis with application to spherical coordinates. *Journal of Geodesy*, *83*, 621–634.

Chesley, S. R., Farnocchia, D., Nolan, M. C., Vokrouhlický, D., Chodas, P. W., Milani, A., Spoto, F., Rozitis, B., Benner, L. A. M., Bottke, W. F., Busch, M. W., Emery, J. P., Howell, E. S., Lauretta, D. S., Margot, J.-L., & Taylor, P. A. (2014). Orbit and bulk density of the OSIRIS-REx target Asteroid (101955) Bennu. *Icarus*, *235*, 5–22. doi:10.1016/j.icarus.2014.02.020. arXiv:1402.5573.

Clark, B. E., Binzel, R. P., Howell, E. S., Cloutis, E. A., Ockert-Bell, M., Christensen, P., Barucci, M. A., DeMeo, F., Lauretta, D. S., Connolly, H., Soderberg, A., Hergenrother, C., Lim, L., Emery, J., & Mueller, M. (2011). Asteroid (101955) 1999 RQ36: Spectroscopy from 0.4 to 2.4 μm and meteorite analogs. *Icarus*, *216*, 462–475. doi:10.1016/j.icarus.2011.08.021.

Drake, M. J., Lauretta, D. S., & Osiris-Rex Team (2011). OSIRIS-REx Asteroid Sample Return Mission. *LPI Contributions*, *1611*, 5012.

Drinkwater, M., Floberghagen, R., Haagmans, R., Muzi, D., & Popescu, A. (2003). GOCE: ESA's first Earth Explorer Core mission. In *Earth gravity field from space – From sensors to earth sciences* (pp. 419–432). Springer.

Freeden, W., & Gerhards, C. (2012). *Geomathematically oriented potential theory*. CRC Press.

Fukushima, T. (2013). Recursive computation of oblate spheroidal harmonics of the second kind and their first-, second-, and third-order derivatives. *Journal of Geodesy*, *87*, 303–309. URL: http://dx.doi.org/10.1007/s00190-012-0599-7. doi:10.1007/s00190-012-0599-7.

Fukushima, T. (2014). Prolate spheroidal harmonic expansion of gravitational field. *The Astronomical Journal*, *147*, 152.

Garmier, R., Barriot, J.-P., Konopliv, A. S., & Yeomans, D. K. (2002). Modeling of the eros gravity field as an ellipsoidal harmonic expansion from the near doppler tracking data. *Geophysical research letters*, *29*, 72–1.

Gil, A., & Segura, J. (1998). A code to evaluate prolate and oblate spheroidal harmonics. *Computer Physics Communications*, *108*, 267–278.

Hobson, E. W. (1931). *The theory of spherical and ellipsoidal harmonics*. Cambridge, Great Britain.

Hotine, M. (1969). *Mathematical geodesy*. ESSA, U.S. Department of Commerce.

Hu, X., & Jekeli, C. (2014). A numerical comparison of spherical, spheroidal and ellipsoidal harmonic gravitational field models for small non-spherical bodies: examples for the Martian moons. *Journal of Geodesy*, (pp. 1–19).

Hudson, R. S., & Ostro, S. J. (1994). Shape of Asteroid 4769 Castalia (1989 PB) from Inversion of Radar Images. *Science*, *263*, 940–943. doi:10.1126/science.263.5149.940.

Jekeli, C. (1988). The exact transformation between ellipsoidal and spherical expansions. *Manuscripta geodaetica*, *13*, 106–113.

Koop, R. (1993). *Global gravity field modelling using satellite gravity gradiometry*. Ph.D. thesis Netherlands geodetic commission, Delft, Netherlands .

Lauretta, D. S., Bartels, A. E., Barucci, M. A., Bierhaus, E. B., Binzel, R. P., Bottke, W. F., Campins, H., Chesley, S. R., Clark, B. C., Clark, B. E., Cloutis, E. A., Connolly, H. C., Crombie, M. K., Delbó, M., Dworkin, J. P., Emery, J. P., Glavin, D. P., Hamilton, V. E., Hergenrother, C. W., Johnson, C. L., Keller, L. P., Michel, P., Nolan, M. C., Sandford, S. A., Scheeres, D. J., Simon, A. A., Sutter, B. M., Vokrouhlický, D., & Walsh, K. J. (2014). The OSIRIS-REx target asteroid (101955) Bennu: Constraints on its physical, geological, and dynamical nature from astronomical observations. *Meteoritics and Planetary Science*, . doi:10.1111/maps.12353.

Lebedev, N. N. (1972). *Special functions and their applications*. Courier Corporation.

Lowes, F. J., & Winch, D. E. (2012). Orthogonality of harmonic potentials and fields in spheroidal and ellipsoidal coordinates: application to geomagnetism and geodesy. *Geophysical Journal International*, *191*, 491–507. URL: http://dx.doi.org/10.1111/j.1365-246X.2012.05590.x. doi:10.1111/j.1365-246X.2012.05590.x.

Maus, S. (2010). An ellipsoidal harmonic representation of Earth's lithospheric magnetic field to degree and order 720. *Geochem. Geophys. Geosyst.*, *11*. doi:10.1029/2010GC003026.

Milani, A., Chesley, S. R., Sansaturio, M. E., Bernardi, F., Valsecchi, G. B., & Arratia, O. (2009). Long term impact risk for (101955) $1999_{RQ}36$. *Icarus*, *203*, 460–471. doi:10.1016/j.icarus.2009.05.029. arXiv:0901.3631.

Neese, C. E. (2004). Small body radar shape models v2.0. *NASA Planetary Data System, EAR-A-5-DDR-RADARSHAPE-MODELS-V2.0*, .

Nolan, M., Magri, C., Howell, E., Benner, L., Giorgini, J., Hergenrother, C., Hudson, R., Lauretta, D., Margot, J., Ostro, S. et al. (2013). Asteroid (101955) bennu shape model v1. 0. *NASA Planetary Data System*, *211*.

Nolan, M. C., Magri, C., Howell, E. S., Benner, L. A. M., Giorgini, J. D., Hergenrother, C. W., Hudson, R. S., Lauretta, D. S., Margot, J.-L., Ostro, S. J., & Scheeres, D. J. (2013). Shape model and surface properties of the OSIRIS-REx target Asteroid (101955) Bennu from radar and lightcurve observations. *Icarus*, *226*, 629–640. doi:10.1016/j.icarus.2013.05.028.

Ostro, S. J., Chandler, J. F., Hine, A. A., Rosema, K. D., Shapiro, I. I., & Yeomans, D. K. (1990). Radar images of asteroid 1989 PB. *Science*, *248*, 1523–1528. doi:10.1126/science.248.4962.1523.

Ostro, S. J., Margot, J.-L., Benner, L. A. M., Giorgini, J. D., Scheeres, D. J., Fahnestock, E. G., Broschart, S. B., Bellerose, J., Nolan, M. C., Magri, C., Pravec, P., Scheirich, P., Rose, R., Jurgens, R. F., De Jong, E. M., & Suzuki, S. (2006). Radar Imaging of Binary Near-Earth Asteroid (66391) 1999 KW4. *Science*, *314*, 1276–1280. doi:10.1126/science.1133622.

Park, R., Konopliv, A., Asmar, S., Bills, B., Gaskell, R., Raymond, C., Smith, D., Toplis, M., & Zuber, M. (2014). Gravity field expansion in ellipsoidal harmonic and polyhedral internal representations applied to vesta. *Icarus*, *240*, 118–132.

Pavlis, N. K., Holmes, S. A., Kenyon, S. C., & Factor, J. K. (2012). The development and evaluation of the Earth Gravitational Model 2008 (EGM2008). *Journal of Geophysical Research (Solid Earth)*, *117*, 4406. doi:10.1029/2011JB008916.

Press, W. H. (2007). *Numerical recipes 3rd edition: The art of scientific computing*. Cambridge university press.

Rektorys, K. e. a. (1994). *Survey of Applicable Mathematics I, II*. Dordrecht-Boston-London, Kluwer.

Ruiz, O., Arroyave, S., & Acosta, D. (2013). Fitting of Analytic Surfaces to Noisy Point Clouds. *American Journal of Computational Mathematics*, *3*, 18–26. doi:10.4236/ajcm.2013.31A004.

Scheeres, D. J., McMahon, J., Takahashi, Y., Chesley, S., & Nolan, M. (2012). Radio Science at 1999 RQ36 for OSIRIS-REx. *LPI Contributions*, *1667*, 6191.

Scheeres, D. J., Ostro, S. J., Hudson, R. S., & Werner, R. A. (1996). Orbits Close to Asteroid 4769 Castalia. *Icarus*, *121*, 67–87. doi:10.1006/icar.1996.0072.

Segura, J., & Gil, A. (1999). Evaluation of associated Legendre functions off the cut and parabolic cylinder functions. *Electronic Transactions on Numerical Analysis*, *9*, 137–146.

Smith, D. E., Zuber, M. T., Phillips, R. J., Solomon, S. C., Hauck, S. A., Lemoine, F. G., Mazarico, E., Neumann, G. A., Peale, S. J., Margot, J.-L. et al. (2012). Gravity field and internal structure of mercury from messenger. *Science*, *336*, 214–217.

Takahashi, Y., & Scheeres, D. (2014). Small body surface gravity fields via spherical harmonic expansions. *Celestial Mechanics and Dynamical Astronomy*, *119*, 169–206. URL: http://dx.doi.org/10.1007/s10569-014-9552-9. doi:10.1007/s10569-014-9552-9.

Takahashi, Y., Scheeres, D. J., & Werner, R. A. (2013). Surface gravity fields for asteroids and comets. *Journal of Guidance, Control, and Dynamics*, *36*, 362–374.

Werner, R. A., & Scheeres, D. J. (1996). Exterior gravitation of a polyhedron derived and compared with harmonic and mascon gravitation representations of asteroid 4769 castalia. *Celestial Mechanics and Dynamical Astronomy*, *65*, 313–344.

Wieczorek, M. A., Neumann, G. A., Nimmo, F., Kiefer, W. S., Taylor, G. J., Melosh, H. J., Phillips, R. J., Solomon, S. C., Andrews-Hanna, J. C., Asmar, S. W. et al. (2013). The crust of the moon as seen by grail. *Science*, *339*, 671–675.

Winch, D. E. (1967). An application of oblate spheroidal harmonic functions to the determination of geomagnetic potential. *Journal of Geomagnetism and Geoelectricity*, *19*, 49–61.

Zuber, M. T., Smith, D. E., Lemoine, F. G., & Neumann, G. A. (1994). The shape and internal structure of the moon from the clementine mission. *Science*, *266*, 1839–1843.